Resource

Cell

Dynamic Imaging of Genomic Loci in Living Human Cells by an Optimized CRISPR/Cas System

Baohui Chen,[1] Luke A. Gilbert,[2,7] Beth A. Cimini,[3,4] Joerg Schnitzbauer,[1] Wei Zhang,[1] Gene-Wei Li,[2,7] Jason Park,[2,5] Elizabeth H. Blackburn,[3] Jonathan S. Weissman,[2,6,7,8] Lei S. Qi,[2,5,8,*] and Bo Huang[1,3,8,*]

[1]Department of Pharmaceutical Chemistry
[2]Department of Cellular and Molecular Pharmacology
[3]Department of Biochemistry and Biophysics
[4]Tetrad Graduate Program
[5]UCSF Center for Systems and Synthetic Biology
[6]Howard Hughes Medical Institute
University of California, San Francisco, San Francisco, CA 94158, USA
[7]Center for RNA Systems Biology, Berkeley, CA 94720, USA
[8]California Institute for Quantitative Biomedical Research (QB3), San Francisco, CA 94158, USA
*Correspondence: stanley.qi@ucsf.edu (L.S.Q.), bo.huang@ucsf.edu (B.H.)
http://dx.doi.org/10.1016/j.cell.2013.12.001

SUMMARY

The spatiotemporal organization and dynamics of chromatin play critical roles in regulating genome function. However, visualizing specific, endogenous genomic loci remains challenging in living cells. Here, we demonstrate such an imaging technique by repurposing the bacterial CRISPR/Cas system. Using an EGFP-tagged endonuclease-deficient Cas9 protein and a structurally optimized small guide (sg) RNA, we show robust imaging of repetitive elements in telomeres and coding genes in living cells. Furthermore, an array of sgRNAs tiling along the target locus enables the visualization of nonrepetitive genomic sequences. Using this method, we have studied telomere dynamics during elongation or disruption, the subnuclear localization of the *MUC4* loci, the cohesion of replicated *MUC4* loci on sister chromatids, and their dynamic behaviors during mitosis. This CRISPR imaging tool has potential to significantly improve the capacity to study the conformation and dynamics of native chromosomes in living human cells.

INTRODUCTION

The functional output of the human genome is determined by its spatial organization and dynamic interactions with protein and RNA regulators. For example, the subnuclear positioning of genomic elements can modulate gene expression, heterochromatin formation, and DNA replication (Misteli, 2007; Misteli, 2013). To elucidate the mechanisms that relate genome function to its spatiotemporal organization, a method to image specific DNA sequences in living cells would be indispensable. So far, such studies have mostly relied on fluorescently tagged DNA-binding proteins. However, because of their fixed target sequence and limited choices of native DNA-binding proteins, this approach has been restricted to imaging artificial repetitive sequences inserted into the genome (Robinett et al., 1996) or specialized genomic elements such as the telomeres (Wang et al., 2008), centromeres (Hellwig et al., 2008), and, in bacteria, H-NS-binding loci (Wang et al., 2011). Imaging arbitrary, endogenous genes and genomic loci remains challenging. Although fluorescence in situ hybridization (FISH) (Langer-Safer et al., 1982; Lichter et al., 1990) brings in target sequence flexibility through base paring of the nucleic acid probes, it is incompatible with live imaging due to sample fixation and DNA denaturation. Thus, we sought to develop a genome-imaging technique that combines the flexibility of nucleic acid probes and the live imaging capability of DNA-binding proteins.

The type II CRISPR (*c*lustered *r*egularly *i*nterspaced *s*hort *p*alindromic *r*epeats) system derived from *Streptococcus pyogenes* (Barrangou et al., 2007; Deltcheva et al., 2011; Wiedenheft et al., 2012) provides a promising platform to accomplish this goal. CRISPR uses a Cas9 protein to recognize DNA sequences, with target specificity solely determined by a small guide (sg) RNA and a protospacer adjacent motif (PAM) (Jinek et al., 2012). Upon binding to target DNA, the Cas9-sgRNA complex generates a DNA double-stranded break. Recent work has demonstrated that by harnessing this RNA-guided nuclease activity CRISPR can be repurposed to edit the genomes of a broad range of organisms (Cong et al., 2013; Mali et al., 2013; Wang et al., 2013). Furthermore, a repurposed, nuclease-deactivated Cas9 (dCas9) protein has been used to regulate endogenous gene expression by controlling the RNA polymerase activity or by modulating promoter accessibility when fused with transcription factors (Gilbert et al., 2013; Qi et al., 2013). Going beyond gene editing and regulation, we

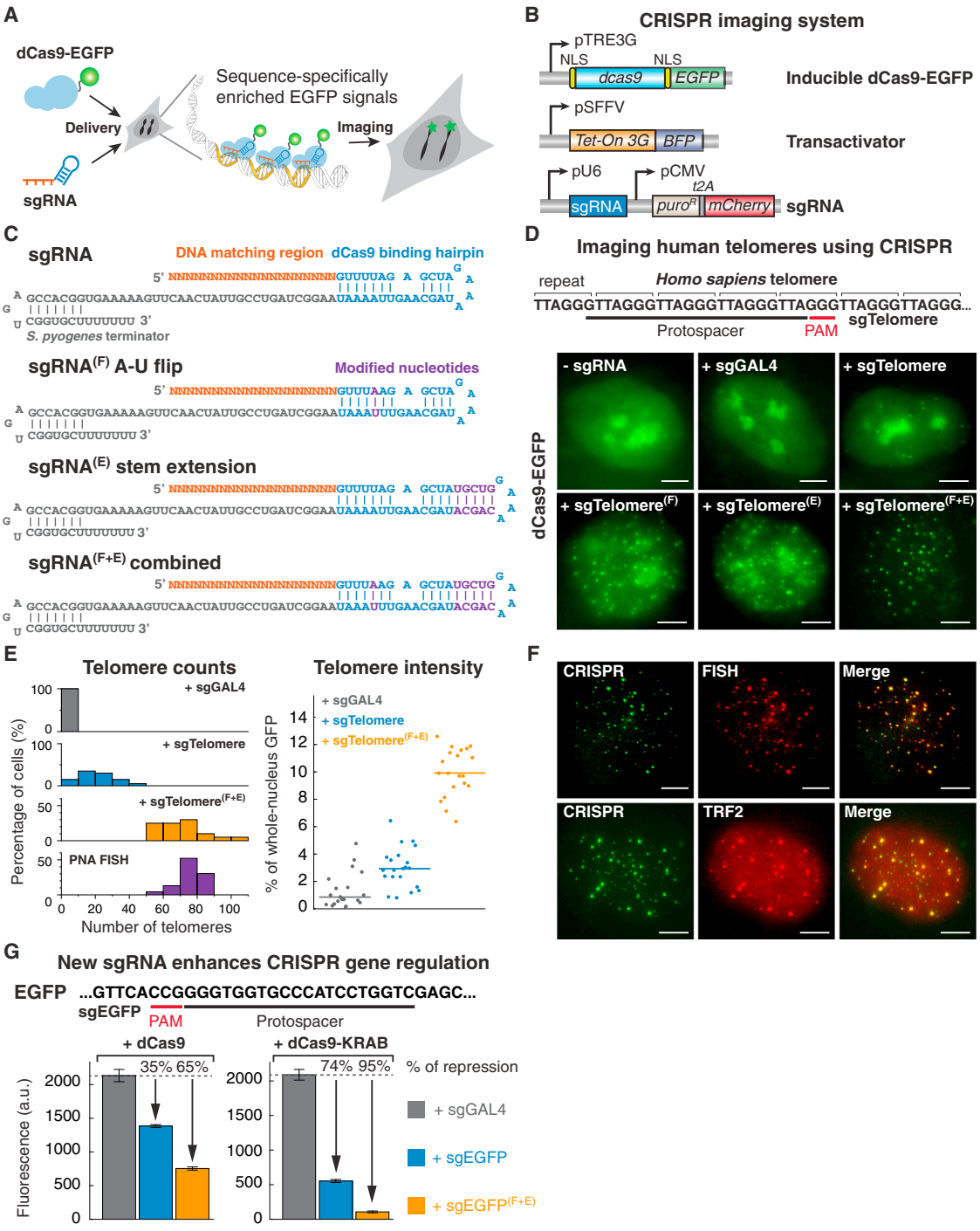

Figure 1. An Optimized CRISPR/Cas System for Visualizing Genomic Sequences in Living Mammalian Cells

(A) Overview of CRISPR imaging. Sequence-specific enrichment of fluorescence signals by sgRNA-directed dCas9-EGFP allows the imaging of genomic elements in living cells.

(B) The three components of the CRISPR imaging: a doxycycline-inducible dCas9-EGFP fusion protein, a Tet-on 3G transactivator, and target-specific sgRNAs expressed from a murine U6 promoter.

(C) Optimized sgRNA designs. sgRNA$^{(F)}$, A-U pair flip; sgRNA$^{(E)}$, a 5 bp extension of the hairpin; sgRNA$^{(F+E)}$, combination of both modifications. Target base pairing region (orange), dCas9-binding hairpin (blue), the *S. pyogenes*-derived terminator (gray), and nucleotide modifications (purple) are shown.

(D) CRISPR imaging of human telomeres in RPE cells using different sgRNA designs. The sgRNA target sequence (black line) and the PAM (red line) are shown. sgGAL4 is used as the negative control.

(legend continued on next page)

sought to use the CRISPR system as a universal and flexible platform for the dynamic imaging of specific genomic elements in living mammalian cells.

Here, we report a CRISPR-based technique for sequence-specific visualization of genomic elements in living human cells. Our imaging system consists of an EGFP-tagged, endonuclease-deactivated dCas9 protein and a structurally optimized sgRNA that improves its interaction with the dCas9 protein. We show that this optimized CRISPR system enables robust imaging of repetitive elements in both telomeres and protein-coding genes such as the Mucin genes in human cells. Furthermore, we use multiple sgRNAs to tile along the target locus to visualize nonrepetitive genomic sequences in the human genome. This CRISPR imaging method allows easy and reliable tracking of the telomere dynamics during telomere elongation or disruption, and enables us to observe chromatin organization and dynamics throughout the cell cycle. The CRISPR technology offers a complementary approach to FISH or the use of DNA-binding proteins for imaging, providing a general platform for the study of native chromatin organization and dynamics in living human cells.

RESULTS

An Optimized CRISPR System Enables Visualization of Telomeres and Enhances Gene Regulation

To engineer the CRISPR system for imaging endogenous genomic sequences, we fused a dCas9 protein lacking the endonucleolytic activity to an enhanced green fluorescent protein (EGFP). Coexpression of dCas9-EGFP and sequence-specific sgRNAs should allow the enrichment of fluorescent signal at the targeted genomic loci for imaging (Figure 1A). To better target the dCas9-EGFP protein into the nucleus, we tested different dCas9 and EGFP fusions carrying two copies of nuclear localization signal (NLS) sequences (Figure S1A available online). A fully nuclear-localized version (#4) was selected (see Extended Experimental Procedures for the dCas9-EGFP sequence). We then created clonal RPE, HeLa, and UMUC3 cell lines that stably expressed dCas9-EGFP from an inducible Tet-On 3G system using lentiviral vectors (Figure 1B). To reduce the background fluorescence that arises from unbound dCas9-EGFP, we performed subsequent imaging experiments at the basal level of dCas9-EGFP expression without doxycycline induction (Figure S1B).

We started by imaging human telomeres, specialized chromatin structures composed of 5 to 15 kb tracts of TTAGGG repeats and associated proteins (Moyzis et al., 1988). Such repeats allow the recruitment of multiple dCas9-EGFP proteins to the same locus using a single sgRNA sequence. Following a previously reported sgRNA design (Jinek et al., 2012; Qi et al., 2013), we created an sgRNA (sgTelomere) containing a 22 nt telomere targeting sequence (Figures 1C and 1D; see Extended Experimental Procedures for sgRNA sequences). We infected stable dCas9-EGFP RPE cells with a lentivirus that expressed sgTelomere from a murine polymerase III U6 promoter (Figure 1B). An sgRNA that had no cognate target in the human genome (sgGAL4) was used as the negative control. At 48 hr postinfection, about 80% sgTelomere-expressing cells showed fluorescent puncta resembling telomeres in addition to bright regions resembling nucleoli. In contrast, sgGAL4-expressing cells only contained nucleolar signal (Figure 1D). Nevertheless, the observed number of telomere puncta, typically 10 to 40 per cell, was substantially lower than the expected telomere number in human cells (146 for our RPE cells, see later karyotyping results), indicating that the system was suboptimal.

Previous work has indicated that the sgRNA expression level limits CRISPR/Cas9 function in human cells (Jinek et al., 2013). Indeed, the observed nucleolus-like signal possibly came from dCas9 proteins that were not bound to sgRNA. Therefore, we modified the sgRNA design to increase its stability and to enhance its assembly with the dCas9 protein (Figures 1C and S1C). To avoid premature termination of U6 Pol-III transcription, we removed a putative Pol-III terminator (4 consecutive U's) in the sgRNA stem-loop by an A-U base pair flip (Figures 1C, sgRNA$^{(F)}$) (Nielsen et al., 2013). To improve sgRNA-dCas9 assembly, we extended the dCas9-binding hairpin structure (Figures 1C, sgRNA$^{(E)}$). Both sgRNA designs produced increased puncta numbers as well as decreased background and nucleolar signals. Further enhanced imaging efficiency was achieved by combining the A-U flip and hairpin extension (Figures 1C and 1D, sgRNA$^{(F+E)}$), which increased the observable puncta number by 2-fold and the signal-to-background intensity ratio by 5-fold (Figure 1E).

To verify the specificity and efficiency of telomere imaging by CRISPR, we performed two-color imaging with telomere-specific FISH using Cy5-tagged peptide nucleic acid (PNA) probes, or with immunofluorescence for endogenous TRF2, a protein in the shelterin complex that binds to the telomeric DNA repeats (Griffith et al., 1999) (Figure 1F). For brighter CRISPR puncta (top 1/3) we observed nearly perfect (95%) colocalization with either PNA or TRF2 puncta. However, we had to use a modified PNA FISH protocol to preserve dCas9-EGFP signal (see Extended Experimental Procedures), which resulted in reduced efficiency for PNA to detect shorter telomeres. The relatively high background of TRF2 immunofluorescence also hindered short telomere detection. Therefore, we measured the total telomere number identified by CRISPR or standard PNA FISH to compare the labeling efficiencies. The two numbers perfectly matched (Figure 1E), indicating a similar efficiency for CRISPR and PNA FISH. In addition, the finding that no puncta were detected in the negative sgGAL4 control suggests a minimal off-target effect for CRISPR imaging.

(E) Histograms of telomere counts and telomere intensity (measured as % of whole-nucleus GFP) in single cell using sgTelomere and sgTelomere$^{(F+E)}$. The telomere number detected by PNA FISH is also shown. n = 20.

(F) Colabeling of telomeres using dCas9-EGFP (green) and PNA FISH (top, red), or dCas9-EGFP and antibody to TRF2 (bottom, red).

(G) Optimized sgRNA design improves gene regulation efficiency using dCas9 alone (left) or dCas9-KRAB fusion protein (right). The target sequence (black line) and the PAM (red line) are shown. The data are displayed as mean ± SD for three independent experiments. All scale bars, 5 μm.

See also Figure S1.

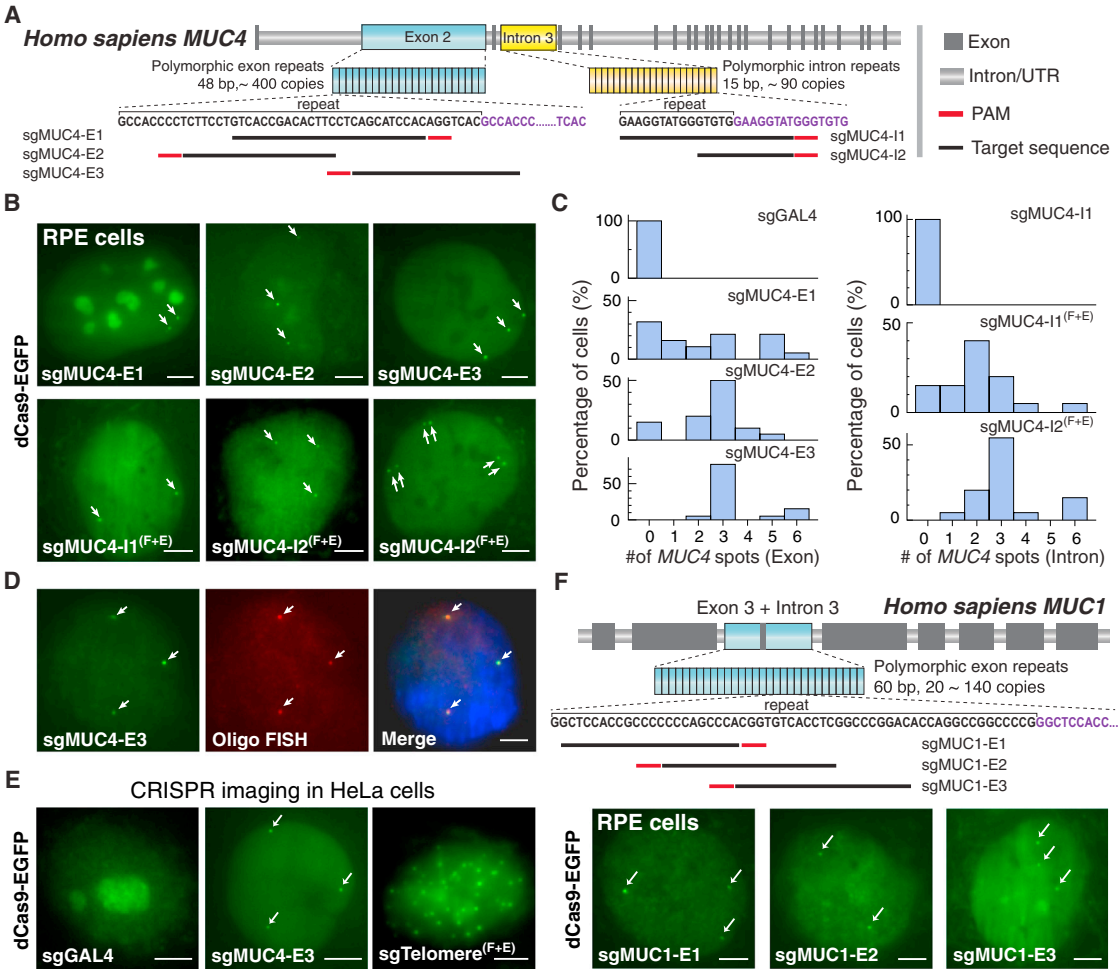

Figure 2. CRISPR Imaging of Endogenous Genes in Different Human Cell Lines

(A) Schematic of the human *MUC4* gene showing two repeated regions in exon 2 (blue) and intron 3 (yellow). The target sequence (black line) and the PAM (red line) are shown.

(B) CRISPR labeling of *MUC4* loci (arrows) in RPE cells by targeting the exon 2 repeats or the intron 3 repeats with different sgRNAs. The arrow pairs in the bottom right image indicate replicated *MUC4* loci.

(C) Histograms of *MUC4* loci counts by CRISPR labeling (n = 20).

(D) Colocalization of dCas9-EGFP labeling (green) and Oligo DNA FISH labeling (red) for *MUC4*.

(E) CRISPR imaging of *MUC4* and telomeres in HeLa cells. sgGAL4 is used as the negative control.

(F) CRISPR labeling of the *MUC1* loci (arrows) in RPE cells. Schematic of the human *MUC1* gene shows the repeat region in exon 3 and intron 3. The target sequence (black line) and the PAM (red line) are shown. All scale bars, 5 μm.

See also Figures S2 and S3.

Interestingly, this optimized sgRNA design also greatly enhanced gene regulation by CRISPR interference (CRISPRi) (Qi et al., 2013). We observed that the new sgRNA$^{(F+E)}$ design significantly improved transcriptional repression of a genomic EGFP reporter in HEK293 cells that stably expressed dCas9 or dCas9-KRAB (Figure 1G). We also tested additional sgRNA designs that consisted of a polymerase-III SINE poly-adenylation signal sequence at the 3′ end, alternative A-U flips, or alternative ways of hairpin extension (Figure S1C). No further improvement of transcriptional repression was observed compared to that in the three designs described above (Figure S1D). Thus, the optimized sgRNA$^{(F+E)}$ design improves efficiencies for both imaging and gene regulation.

CRISPR Imaging Allows Visualization of Repetitive Sequences in Endogenous Protein-Coding Genes

To expand the applications of CRISPR imaging, we tested whether we could use CRISPR to image protein-coding genes. Specifically, we chose the *MUC4* gene on chromosome 3 that encodes a glycoprotein important for protecting mucus in diverse epithelial tissues and during tumor formation (Hollingsworth and Swanson, 2004). The *MUC4* gene contains a region with variable number tandem repeats (100 to 400 repeats of a 48 bp sequence) in the second exon (Figure 2A) (Nollet et al., 1998). To image the *MUC4* exon, we designed three sgRNAs (see Extended Experimental Procedures for sgRNA sequences) targeting this repetitive region (sgMUC4-E1, E2, and E3). We

observed that the labeling efficiency depended on the target site. The best one, sgMUC4-E3, showed two or more puncta in all cells even when the original sgRNA design was used (Figures 2B and 2C). We confirmed the specificity of the CRISPR signal by colabeling with oligo-DNA FISH of the same repetitive region in fixed cells (Figure 2D, see Extended Experimental Procedures for DNA-FISH probe sequence).

The *MUC4* gene also contains ~90 repeats of a 15 bp sequence in the third intron. For this tract, we designed two sgRNAs with different lengths of complementarity (23 bp and 13 bp). In this case, the sgRNA$^{(F+E)}$ design was critical for visualizing the *MUC4* intron (Figures 2B and 2C). Surprisingly, the 13 nt sgMUC4-I2$^{(F+E)}$ showed higher labeling efficiency, suggesting that its DNA-binding affinity might not be lower than that of the longer sgMUC4-I1$^{(F+E)}$, as both sgRNAs have a footprint of two 15 bp repeats with the 3 nt PAM included. This result possibly suggests a shorter sgRNA base pairing length requirement for imaging compared to that for efficient gene editing or gene regulation (Jinek et al., 2012; Qi et al., 2013).

We noticed that increasing the dosage of sgRNA lentivirus could reduce the nucleolar signal from dCas9-EGFP. For example, for both *MUC4* and telomere labeling, infecting cells with 1:3-diluted lentivirus effectively reduced the nucleolar signal (Figure S2A). Furthermore, the optimized sgRNA$^{(F+E)}$ design not only allowed efficient labeling of target sites using a lower viral dosage (Figure S2B), but also decreased the nucleolar signal (Figure S2C). These observations further confirmed that sgRNA is a limiting factor for CRISPR imaging: low expression or suboptimal design potentially contributes to off-target clustering of dCas9-EGFP in nucleoli.

We saw three labeled *MUC4* loci in the majority of cells by both exon and intron labeling. Indeed, whole-cell karyotyping revealed aneuploidy of our RPE cell line (Figure S3A), and chromosome 3 trisomy was further confirmed by FISH staining of two different regions on chromosome 3 (Figure S3B). Concomitantly, in ~15% of cells, we also observed six CRISPR puncta with either *MUC4* exon or intron labeling, suggesting that these cells had replicated these genomic loci (Figures 2B and 2C). These results demonstrated that CRISPR imaging is capable of detecting gene copy numbers in living cells.

To demonstrate the generality of CRISPR imaging in different cell types, we imaged telomeres and *MUC4* in HeLa cells using sgTelomere$^{(F+E)}$ and sgMUC4-E3. In both cases, we observed effective labeling of the target genomic loci (Figure 2E). We similarly observed three copies of *MUC4* loci in our HeLa cell line. FISH experiments confirmed that these cells were also trisomic for chromosome 3 (Figure S3B). To test the ability to image repetitive elements in other genes, we designed sgRNAs to visualize the *MUC1* gene on chromosome 1 (Figure 2F) (Gendler et al., 1990). The *MUC1* gene contains a polymorphic region with a variable number of 60-bp repeats in the third exon and intron, and the sgRNAs were designed to target within each repeat (sgMUC1-E1, E2, E3). We similarly observed multiple distinct *MUC1* loci in RPE cells, and again observed that the labeling efficiency varied by target sequences.

To test whether CRISPR imaging affects gene expression, we performed qPCR to quantify *MUC4* transcription in RPE cells labeled with sgMUC4-E1, sgMUC4-E3$^{(F+E)}$, sgMUC4-I2$^{(F+E)}$, or both sgMUC4-E3$^{(F+E)}$ and sgMUC4-I2$^{(F+E)}$ (Figure S3C). Only in the presence of both sgMUC4-E3$^{(F+E)}$ and sgMUC4-I2$^{(F+E)}$, a weak (~45%) repression was observed. This phenomenon is consistent with previous observations that targeting downstream sequences of the transcription start site is less effective for CRISPRi gene silencing (Qi et al., 2013). In contrast, labeling *MUC1* using sgMUC1-E1$^{(F+E)}$ or sgMUC1-E3$^{(F+E)}$ both repressed *MUC1* transcription by ~80% (Figure S3D), likely due to the fact that the target sites were close (~1 kb) to the transcription start site. Thus, although CRISPR imaging may perturb gene expression, this perturbation could be minimized by targeting the far downstream region or upstream region of the promoter (but not the enhancers).

CRISPR Allows Imaging of Arbitrary Nonrepetitive Genomic Sequences

Most sequences in the human genome are nonrepetitive. Unlike other DNA-binding proteins, the target specificity of dCas9 is determined by sgRNA, which allows easy labeling of nonrepetitive sequences by targeting multiple adjacent sites with a single dCas9 protein. To demonstrate this capability of CRISPR to image nonrepetitive genomic loci, we designed 73 sgRNAs targeting both DNA strands spanning a 5 kb nonrepetitive region in the first intron of *MUC4* gene (Figure 3A, see Extended Experimental Procedures for target sequences). We produced lentiviral cocktails, each containing 5 to 6 sgRNAs, and infected different numbers of sgRNAs (16, 26, 36, or 73) into RPE cells. The total virus dosage was twice as much as used for repetitive sequence imaging. We observed effective labeling of the *MUC4* loci using 36 sgRNAs. Increasing the number of sgRNAs to 73 did not improve the labeling efficiency, but reducing the sgRNA number to 16 resulted in no detectable puncta (Figures 3A and 3B). Our results suggest that 26 to 36 sgRNAs are sufficient to detect a nonrepetitive genomic locus using CRISPR. Further reduction of the required number of sgRNAs could be implemented by decreasing the background level of dCas9-EGFP or improving the imaging sensitivity (Gaj et al., 2013).

We also used multiple sgRNAs to colabel either the same *MUC4* gene or both *MUC1* and *MUC4* genes. Labeling the *MUC4* gene using two sgRNAs, sgMUC4-E3 and sgMUC4-I2$^{(F+E)}$, did not result in more puncta compared to using sgMUC4-E3 alone (Figure 3C), which can be explained by the close proximity (~1 kb) of these two loci. In contrast, using both sgMUC4-E3 and sgMUC1-E1 led to 6 to 9 puncta observed in 45% of cells (Figure 3D). Unlike the *MUC4*-only images where the six puncta formed pairs, the *MUC1*+*MUC4* images showed mostly unpaired spots. These results demonstrate the potential of using CRISPR for the simultaneous and multiplexing labeling of many genomic elements.

CRISPR Imaging Monitors Telomere Length

The ability of using CRISPR to label telomeres prompted us to test whether it allowed direct detection of the telomere length in living cells. Indeed, in two-color images of telomeres in RPE cells (Figure 1F), the intensity of individual telomere puncta detected using CRISPR and PNA FISH showed good linear correlation (Figure S4A). Linear correlation was also found between CRISPR labeling and TRF2 immunolabeling of the telomeres (Figure S4B).

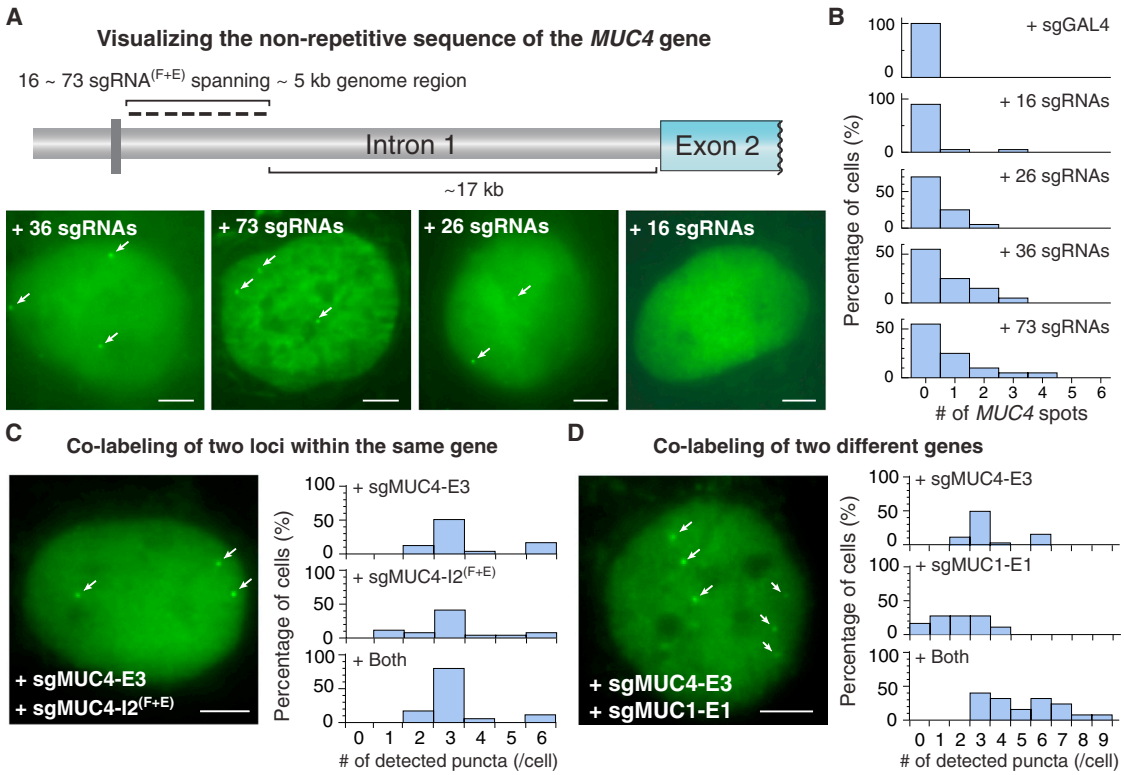

Figure 3. CRISPR Imaging of Nonrepetitive Genomic Sequences and Multiple Gene Loci

(A) CRISPR labeling of the nonrepetitive region of *MUC4* intron 1 using multiple optimized sgRNAs. With 26, 36, or 73 sgRNAs, 1 to 3 spots (arrows) can be detected.

(B) Histograms of *MUC4* loci counts by CRISPR imaging of the nonrepetitive *MUC4* sequence.

(C) Colabeling of the *MUC4* exon 2 and intron 3. The physical proximity (~1 kb) of the two target regions does not increase the puncta number as shown in the histograms.

(D) Colabeling of *MUC1* and *MUC4* genes. Labeling two distal genes (*MUC1* on chromosome 1 and *MUC4* on chromosome 3 respectively) increases the puncta count as shown in the histograms (n = 20). All scale bars, 5 μm.

See also Movie S3.

Although two-color imaging directly assesses whether CRISPR intensity accurately measures the length of individual telomeres, these experiments had the caveats of low efficiency in detecting short telomeres by TRF2 immunofluorescence and our modified PNA FISH protocol. Therefore, we also analyzed the median telomere puncta intensity labeled by CRISPR imaging or by PNA FISH, a common method for quantifying telomere length (Figure 4A) (Hultdin et al., 1998). We compared telomere images of RPE cells and those of the UMUC3 human bladder cancer cell line. The median CRISPR puncta intensity in RPE cells was 3.1 times as high as that in UMUC3 cells, which exactly matched the intensity ratio measured by PNA FISH (Figure 4A). In both RPE and UMUC3 cells, we detected similar numbers of telomeres using CRISPR imaging or PNA FISH (Figures S4C). Moreover, the telomere length in UMUC3 cells can be conditionally elongated by transfection with a human telomerase RNA (hTR) gene (1.6 to 5 kb without hTR; 3 to 10 kb with hTR) (Xu and Blackburn, 2007). In this study, 6 days after hTR lentiviral infection, we detected a 63% increase of median PNA FISH intensity, while the median CRISPR intensity also increased by 28% (Figure 4B). The correlation of both measured intensity and telomere counts suggests that CRISPR imaging is a method comparable to PNA FISH for detecting telomere length, with the added feature of labeling in living cells.

CRISPR Imaging Monitors Telomere Dynamics

CRISPR imaging offers a unique platform to track native genetic elements in living cells without introducing artificially inserted sequences. We performed high-frequency (0.2 s per frame) time-lapse microscopy to track the movement of telomeres in living RPE cells. Single-particle tracking revealed the confined diffusion of telomeres, which is occasionally overlaid with a slow directed motion (Figure 5A and Movie S1). To test whether CRISPR labeling could affect telomere dynamics, we compared telomere movement labeled by CRISPR or TRF1, one of the major telomeric-binding proteins (Wang et al., 2008). We saw very similar mean-squared displacement (MSD) curves using two methods, demonstrating that CRISPR does not disrupt telomere dynamics (Figure 5B). The microscopy diffusion coefficient of individual telomeres displayed a negative correlation with the fluorescence intensity (Figure 5C), which is consistent with the

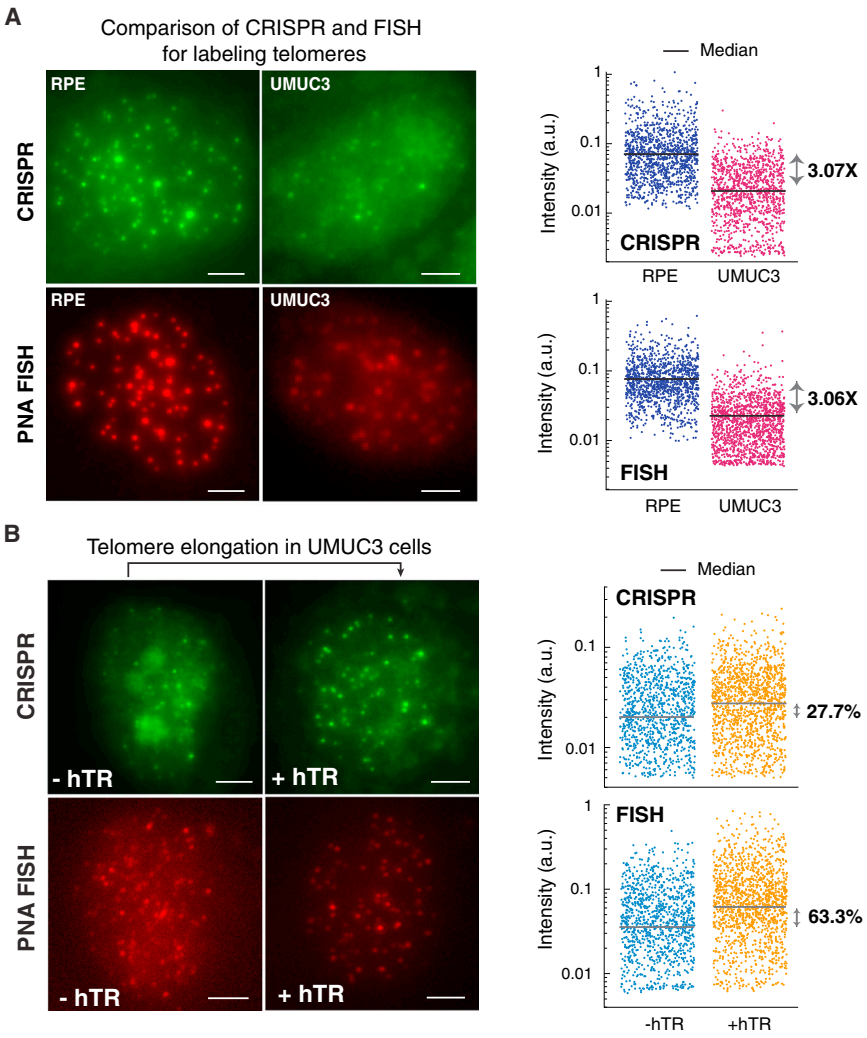

Figure 4. CRISPR Imaging Detects Telomere Length

(A) Comparison of telomere length in RPE and UMUC3 cells using CRISPR imaging (upper) or PNA FISH (lower). The log-scale scatter plot displays the intensity of each identified telomere in RPE (navy) and UMUC3 (purple) cells.

(B) hTR-induced telomere elongation in UMUC3 cells visualized by CRISPR (upper) or PNA FISH (lower). The log-scale scatter plot displays the intensity of each identified telomere without (orange) and with (blue) hTR expression. At least 20 cells were analyzed for each case. All images are maximum z projections. All scale bars, 5 μm. See also Figure S4.

previous study showing that longer telomeres have slower movement (Wang et al., 2008), This result was further supported by our tracking of telomeres in UMUC3 cells, wherein the elongation of telomeres by hTR overexpression induced a slow-down of telomere movement (Figure 5D).

As telomere damage has previously been shown to enhance telomere movement, likely to facilitate DNA repair (Dimitrova et al., 2008; Wang et al., 2008), we examined the movement of telomeres after shRNA knockdown of TIN2, which disrupts the telomere shelterin complex (Kim et al., 1999). We confirmed the resulting DNA damage localized to telomeres by immunostaining of 53BP1, a protein recruited to sites of DNA damage (d'Adda di Fagagna et al., 2003) (Figure S5A). We note that dCas9 binding did not apparently affect telomere integrity because we observed an almost negligible increase in telomerically localized 53BP1 compared to TIN2 knockdown (Figures S5A and S5B). As shown by the MSD curves detected by CRISPR (Figure 5E), we saw an expected increase in microscopic diffusion speed after TIN2 knockdown but not with a scrambled shRNA as the negative control. Simultaneous overexpression of exogenous TIN2 alleviated the DNA damage and restored near-wild-type telomere movement. These results demonstrate the power of CRISPR to directly visualize the movement of endogenous genomic elements.

CRISPR Imaging Reveals the Organization and Dynamics of *MUC4* Loci

In addition to special genetic elements such as the telomere, CRISPR imaging also allows us to examine the spatiotemporal dynamics of protein-encoding DNA sequences in live cells. By tagging *MUC4* exon 2 and intron 3 simultaneously using two sgRNAs, we measured the position of *MUC4* loci by approximating the shape of the nucleus as an oval (Figure 6A). The distribution of normalized *MUC4* radial position peaked near the nuclear envelope (Figure 6B), indicating that *MUC4* loci preferentially locate at the nuclear periphery. Furthermore, by calculating the angle between any two *MUC4* loci (Figure 6C), we found that *MUC4* loci exhibited polarized spatial organization, with the three allelic loci clustering in the same half of the nucleus. These live-cell observations support the notion of nonrandom spatial organization of genes and chromosomes (Cremer and Cremer, 2010).

Next, we monitored the movement of *MUC4* loci (Figure 6D and Movie S2). Similar to telomeres, trajectories of these loci displayed confined movement at short (<5 s) time scales, with additional macroscopic diffusion or directional transport observed over longer time scales (Figure S6A). The short-time-scale confinement sizes and the microscopic diffusion coefficients were highly heterogeneous (Figures 6E, S6B, and S6C). The median values of both parameters were comparable to those measured using LacO arrays on bacterial artificial chromosomes in CHO cells (Levi et al., 2005). Using 36 sgRNAs simultaneously, we also performed live imaging of nonrepetitive sequences of the *MUC4* gene. Despite slightly lower signal, we observed similar movement behaviors, comparable to the movement of repetitive sequences of *MUC4* (Movie S3).

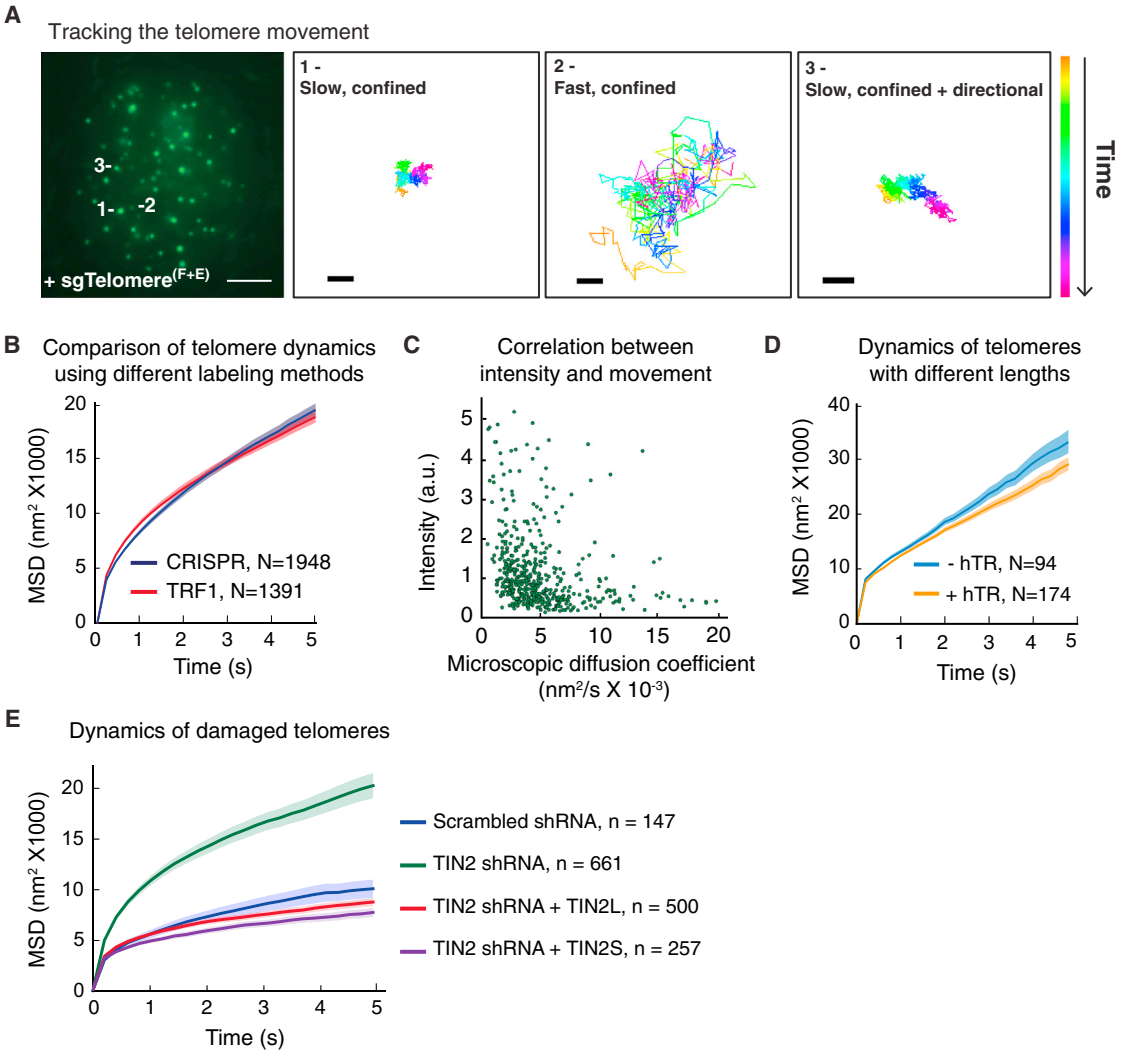

Figure 5. Tracking of Telomere Dynamics in Live Cells by CRISPR Imaging

(A) CRISPR imaging of telomeres in RPE cells (scale bar, 5 μm) and trajectories of three telomeres with different movement modes (scale bars, 200 nm). The trajectory lengths are 600 frames for 1 and 3 and 260 frames for 2. See Movie S1.

(B) Comparison of telomere dynamics using CRISPR (blue) and EGFP-TRF1 (red) labeling in RPE cells. The data are displayed as mean ± SE.

(C) Scatter plot of the CRISPR foci intensity and their microscopic diffusion coefficients.

(D) The average MSD curves of telomeres in UMUC3 cells without (blue) and with (orange) hTR. The data are displayed as mean ± SE.

(E) Averaged MSD curves of CRISPR-labeled telomeres in RPE cells measured with scrambled shRNA (blue), TIN2 shRNA (green), or coexpression of TIN2 shRNA and the long (L, red), or short (S, purple) isoform of TIN2. At least 15 cells are analyzed in each case. The data are displayed as mean ± SE.

See also Figure S5 and Movie S1.

Finally, we characterized replicated *MUC4* loci during late S phase and G2 phase, which appeared as closely located pairs of dCas9-GFP puncta (Figure 6F and Movie S3). The distance between such paired *MUC4* loci on sister chromatids often reached over 1 μm (Figure 6G) and was similar for all three pairs within the same cell (Figure 6F). Although each individual *MUC4* punctum in the pair underwent fast diffusive movement (Movie S4), the pair distance remained relatively constant over several hours (Figure 6H). These results suggest a stable but dispersed distribution along the genomic DNA of factors such as cohesin, which physically holds the two sister chromatids together (Nasmyth and Haering, 2009).

CRISPR Imaging Reports Chromosome Dynamics during Mitosis

By labeling specific genomic loci with dCas9-EGFP, we could also investigate chromosome reorganization during cell division. For this purpose, we tagged *MUC4* exon 2 and intron 3 simultaneously in HeLa cells. Using time-lapse imaging, we recorded cell division from G2 through cytokinesis (Figure 7A and Movie S5). To examine the detailed relationship between the *MUC4* loci and the chromosomes, we stained fixed HeLa cells with DAPI and performed two-color imaging to capture cells at different stages of mitosis (Figure 7B). During prophase and metaphase, *MUC4* puncta localized to the end of the

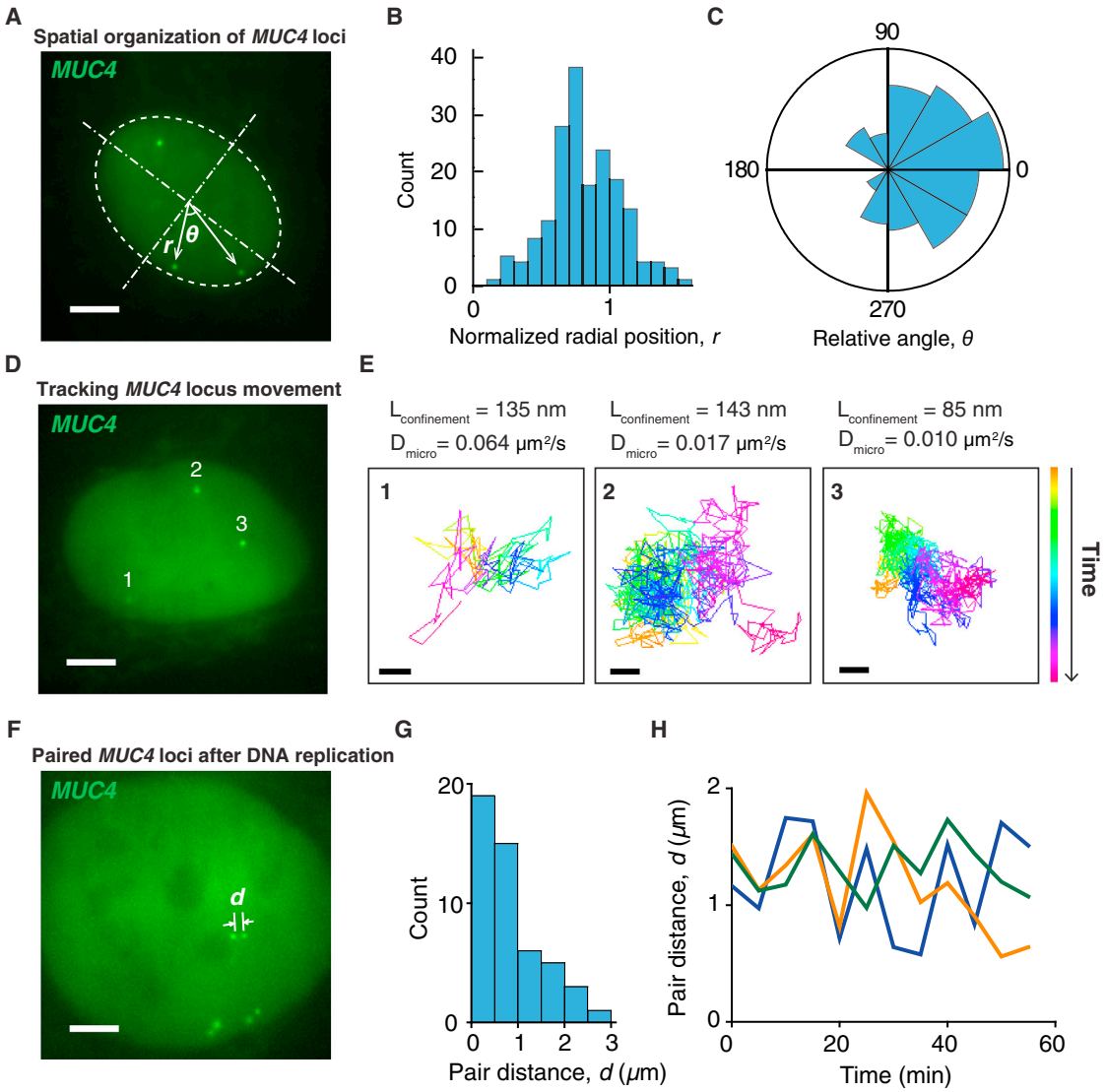

Figure 6. Spatial Organization and Dynamics of the *MUC4* Gene in RPE Cells

(A) Scheme for analyzing the nuclear localization of the *MUC4* gene using both sgMUC4-E3 and sgMUC4-I2$^{(F+E)}$. The nucleus is modeled as an oval and then normalized to a round circle to measure *MUC4* positions.

(B) The histogram of the normalized *MUC4* radial position, *r*. The nuclear envelope is at the unity position.

(C) The histogram of the relative angle of *MUC4* loci with respect to the center of the nucleus, θ. Fifty cells are analyzed for (B) and (C).

(D) Single-particle tracking of *MUC4* loci movement. See Movies S2 and S3.

(E) Trajectories of the three loci in (D), which show different confinement sizes, $L_{confinement}$, and microscopic diffusion coefficients, D_{micro} (scale bars, 200 nm). The trajectory lengths are 900 frames for 2 and 3 and 115 frames for 1.

(F) Paired *MUC4* loci after DNA replication. See Movie S4.

(G) Histogram of the distance between two *MUC4* loci in a pair. Twenty cells are analyzed.

(H) Long-term 3D tracking to measure the pair distances of three *MUC4* pairs within a cell.

(A), (D), and (F) are 20-frame averages of live recording images. Scale bars, 5 μm. See also Figure S6 and Movies S2 and S4.

chromosome arm, precisely reflecting the telomere-proximal position of the *MUC4* gene (at 195.5 Mb on the ~200 Mb chromosome 3). The separation of the two *MUC4* puncta on sister chromatids was discernible but small, indicating that chromosome arm cohesion was maintained during metaphase (Onn et al., 2008). Separation of the pairs of *MUC4* puncta initiated at anaphase. As the result of the symmetric separation of sister chromosomes, in telophase, the position of *MUC4* loci at the two poles of the spindle nearly mirrored each other. This mirror-image relationship was maintained when the two daughter cells formed in both fixed and live-cell experiments (Figure 7). This phenomenon could lead to further studies of the mirror symmetry of initial chromosome packaging in the two daughter cells (Gerlich et al., 2003).

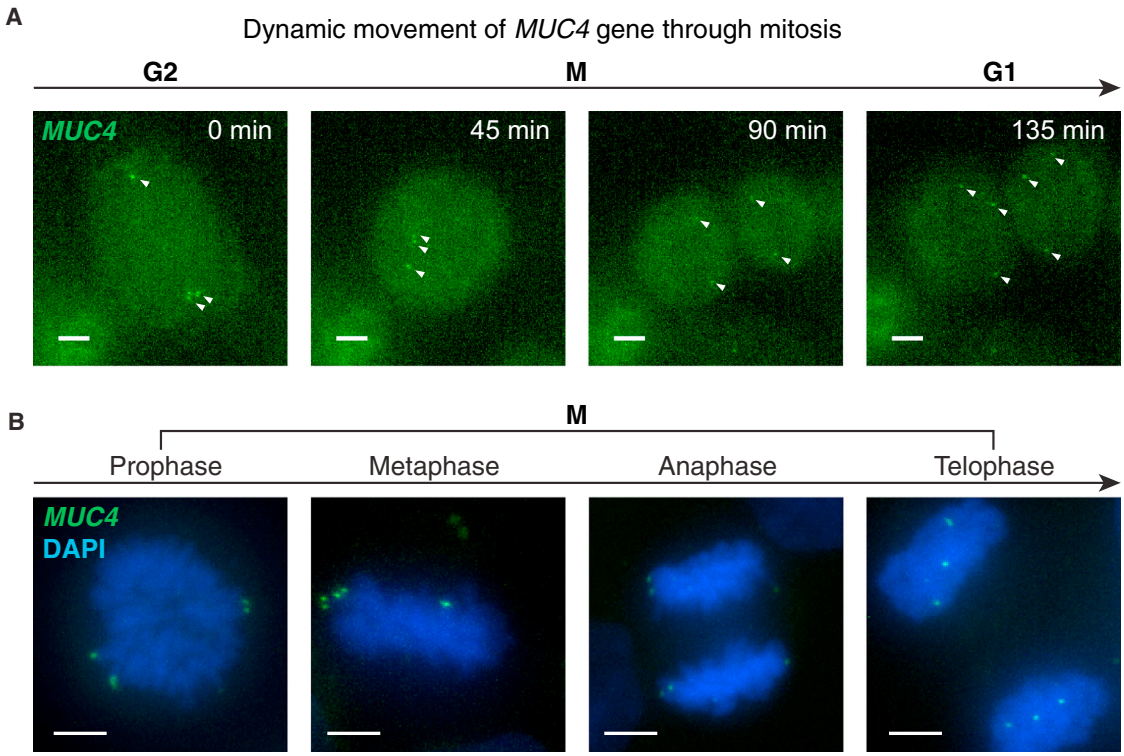

Figure 7. Dynamics of the *MUC4* Loci through Mitosis

(A) Snapshots from a *MUC4* image sequence in which a HeLa cell undergoes mitosis, showing z maximum projections of 4 μm depth. The arrows indicate the *MUC4* loci, which are not completely captured during mitosis because the cell thickness exceeds the z range. See Movie S5.

(B) CRISPR labeled HeLa cells fixed and stained with DAPI (blue) to image the relationship between *MUC4* loci (green) and the chromosomes. Cells at different stages of mitosis are displayed, showing z maximum projections of 18 μm. Scale bars, 5 μm.

See also Movie S5.

DISCUSSION

CRISPR Provides a Robust and Flexible Platform for Dynamic Visualization of Arbitrary Genomic Sequences

Systematic characterization of the relationship between genome spatiotemporal organization and its functional output depends on the ability to visualize genomic elements in living cells. Here we report an imaging technique based on an optimized CRISPR/Cas system to fluorescently label specific genomic loci. We have shown that, simply by using site-specific sgRNAs, an EGFP-tagged dCas9 allows highly flexible and effective detection of both repetitive and nonrepetitive elements in the human genome. This genomic labeling by CRISPR is non-destructive, allowing the observation of native chromatin dynamics. Our data suggest that CRISPR imaging enables a new approach to study chromatin conformation and dynamics in both short time frames and long-term processes such as mitosis.

While FISH requires denaturation of the DNA and is thus incompatible with live imaging, CRISPR imaging allows direct recording of real-time dynamic events. With flexible DNA sequence recognition, CRISPR imaging does not rely on targeted insertion of artificial sequences such as LacO or TetO arrays, which are often challenging to implement and maintain. Compared to transcription activator-like effector (TALE) based systems that have recently been applied to image repetitive sequences in telomere and satellite DNA (Miyanari et al., 2013), the Watson-Crick base pairing mechanism for CRISPR targeting makes our method powerful enough to detect nonrepetitive sequences. The target sequence flexibility of CRISPR may enable genome-wide imaging studies in living cells. Although previous studies have reported off-target binding and editing of the CRISPR system in the human genome (Hsu et al., 2013), our method could filter such sporadic off-target events through a local enrichment of the fluorescence signal. This conclusion is supported by our observation of no puncta in the sgGAL4 negative control. As an even stronger piece of evidence, none of the *MUC4* or *MUC1* images contained a puncta number higher than the actual gene copy number despite the wide variety of sgRNAs used.

The Improved CRISPR System Enhances the Efficiency of Imaging, Gene Regulation, and Likely Genome Editing

Our CRISPR imaging technique has also provided opportunities to understand and improve the CRISPR system itself. In our experiments, we revealed that unbound dCas9 is enriched in the nucleolus, presumably by nonspecific interaction with other RNAs or genomic loci. Such nucleolar signal was reduced by using ours optimized sgRNA design for more efficient expression

and better assembly with the dCas9 protein. This observation provides strong evidence that a major limitation of CRISPR efficacy in mammalian cells is sgRNA stability and folding. Furthermore, the redesigned sgRNA also improved the CRISPRi effects by up to 5-fold. It is possible that this new sgRNA, by eliminating nonspecific binding in the nucleolus, can also improve the efficacy for gene editing, with less off-target effects.

Cas9 variants from different bacterial species pair only with their cognate guide RNAs, and each guide RNA can be designed to recognize a distinct target sequence (Esvelt et al., 2013). Fusion of dCas9 variants with different fluorescent proteins therefore should allow labeling of multiple genomic sequences within a genome, enabling multicolor imaging for multiplexed detection of genetic events. Future engineering of the CRISPR system may also enable the detection of RNAs in addition to genomic DNAs.

CRISPR Imaging Allows Direct Visualization of Genetic Element Dynamics

As demonstrated by our analysis of *MUC4* loci position distribution (Figure 6A), a straightforward application of CRISPR imaging is to monitor the position of specific genomic loci in the nucleus, which is an important mechanism for gene regulation (Misteli, 2007). While this measurement has been traditionally done by FISH or LacO labeling (Heun et al., 2001), CRISPR imaging enables continuous tracking of endogenous loci over a long time period. Colocalization analysis with other nuclear landmarks such as transcription factories, nuclear pore complex, nuclear lamina, and heterochromatin markers may provide further insights into how the spatial organization of genes regulates its expression.

The uncovering of the aneuploidy of our RPE and HeLa cell lines by CRISPR imaging (Figure 2) illustrates its capability to monitor the gene copy number in living cells. This ability could provide a way to visualize gene deletions or duplications, events commonly occurring in cancers. Transposition and chromosome translocation events (Roukos et al., 2013) could conceivably also be recorded.

The human genome contains large numbers of repetitive elements such as telomeres, centromeres, and satellite DNAs. Our study has shown the application of CRISPR imaging to follow the dynamics of telomeres during telomere elongation (Figure 4). Previously, such live telomere experiments have relied on introduction of fluorescently tagged telomere-binding proteins such as TRF1 (Wang et al., 2008), which could potentially perturb binding or localization of other proteins in the same complex. The same is true for imaging centromeres and other genomic loci bound by multi-protein complexes. CRISPR imaging allows direct detection of these loci without overexpression of individual DNA-binding components, avoiding perturbation of the stoichiometry.

CRISPR Imaging Provides a Powerful Tool to Study Chromatin Architecture and Nuclear Organization

How chromatin ultrastructure regulate gene expression is an unsolved question in cell biology. Given our capability to simultaneously label multiple positions within the same *MUC4* gene locus (Figure 3C), we should be able to characterize the local compaction state of the labeled chromatin segment. Such experiments have previously been limited to LacO-labeled bacterial artificial chromosomes (Sinclair et al., 2010). In contrast, CRISPR imaging will shed light on the packaging of endogenous genomic loci and may eventually enable mapping of the whole genome with an sgRNA library. Superresolution microscopy will further unveil sequence-specific chromatin ultrastructure. Of note, our imaging of the highly heterochromatic telomeres also suggests that dCas9 can access heterochromatin regions of the genome. Therefore, CRISPR imaging offers a powerful tool to understand the control of heterochromatin formation (Grewal and Jia, 2007). For example, at the whole-chromosome scale, CRISPR imaging can be instrumental in the study of X chromosome inactivation (Augui et al., 2011; Meyer, 2010).

Our simultaneous imaging of *MUC1* and *MUC4* gene loci (Figure 3D) illustrates the capability of CRISPR imaging to monitor the spatial relationship between different genomic elements. In many cases, long-range DNA interactions are involved in regulating gene expression (Fraser and Bickmore, 2007). CRISPR imaging provides an opportunity to visualize such interactions between a target gene and distant regulatory elements, allowing investigation of the underlying driving forces. Such studies will be further enhanced by the development of multicolor imaging capability. For this application, CRISPR imaging is fully complementary to chromatin conformation capture (3C) and its derived methods 5C, hi-C, etc. (van Steensel and Dekker, 2010). Although CRISPR imaging has lower sequence throughput and sequence resolution, it readily measures individual cell-to-cell variations and adds superior spatiotemporal resolution.

Using CRISPR imaging, we have imaged the *MUC4* loci at different times through the cell cycle. We were able to distinguish replicated *MUC4* loci, the pairing of sister chromatid *MUC4* loci, and the dynamics of *MUC4* loci during mitosis. These observations may allow the measurement of replication timing, sister chromatid cohesion, as well as chromosome condensation and decondensation during mitosis. Labeling different genomic loci with CRISPR could map specific DNA sequences for genomic organization during cell division. Moreover, studies of homologous pairing and recombination in meiosis should also be amenable using this approach.

A Unified CRISPR System for Genome Engineering Including Editing, Regulation, and Imaging

CRISPR has recently been developed for genome editing and gene expression in a broad range of organisms. In addition to modifying the genome sequence and modulating gene expression, here we add another application of CRISPR: its use to directly image the spatial organization and temporal interactions of chromatin. The use of the same type II CRISPR system might greatly simplify the rules and efforts for different tasks in genome engineering and imaging, as the same set of sgRNAs can be modularly combined with different versions of Cas9—a nuclease Cas9 (genome engineering), a transcription factor-fused dCas9 (gene regulation), or a fluorescent protein-tagged dCas9 (live chromatin imaging). Furthermore, with the characterization of orthogonal Cas9 proteins, it is possible to create a unified CRISPR platform for using different Cas9s and cognate sgRNAs to perform these various tasks of genomic manipulation and

observation in the same cell. We believe that such molecular tools will be invaluable to understand, interrogate, and engineer genomes, and are suitable for numerous applications for biomedical research and clinical therapies.

EXPERIMENTAL PROCEDURES

Plasmid Construction

The DNA sequence encoding the dCas9 gene with inactivating D10A and H840A mutations was fused with EGFP and two copies of SV40 NLS. Using standard ligation-independent cloning, we cloned these fusion proteins into a lentiviral vector containing an inducible promoter P_{TRE3G} (Tet-on 3G inducible expression system, Clontech). sgRNAs were cloned into a lentiviral U6-based expression vector derived from pSico, which coexpresses mCherry and a puromycin resistance cassette from a CMV promoter (Larson et al., 2013). For sgRNA design and cloning, see Extended Experimental Procedures for details.

Cell Culture

Human embryonic kidney (HEK) cell line HEK293T, human renal cancer cell line UMUC3 and HeLa cells were maintained in Dulbecco's modified Eagle medium (DMEM) with high glucose (UCSF Cell Culture Facility) in 10% Tet-system-approved FBS (Clontech). Human retinal pigment epithelium (RPE) cells were maintained in DMEM with GlutaMAX1 (Life Technologies) in 10% Tet-system-approved FBS. All cells were maintained at 37°C and 5% CO_2 in a humidified incubator.

Lentiviral Production and Stable Expression of dCas9 and sgRNA

For viral production, HEK293T cells were seeded into T75 flask 1 day prior to transfection. One microgram of pMD2.G plasmid, 8 μg of pCMV-dR8.91, and 9 μg of the lentiviral vector (Tet-on 3G, dCas9-EGFP, GFP-TRF1, sgRNA, or TIN-2 shRNA) were cotransfected into HEK293T cells using FuGENE (Promega) following the manufacture's recommended protocol. Virus was harvested 48 hr posttransfection. For viral transduction, cells were incubated with culture-medium-diluted viral supernatant supplemented with 5μg/ml polybrene for 12 hr. RPE, UMUC3, and HeLa cell lines stably expressing dCas9-EGFP were generated by coinfecting cells with a lentiviral cocktail containing viruses encoding both dCas9-EGFP and the Tet-on 3G transactivator protein (Clontech). Clonal cell lines expressing dCas9-EGFP were generated by picking a single-cell colony. The clones with low basal level expression of dCas9-EGFP were selected for CRISPR imaging. See Extended Experimental Procedures for details.

Gene Regulation Assay

One microgram of each sgRNA plasmid was transfected into 50,000 HEK293 cells stably expressing both the SV40-GFP reporter, and dCas9-BFP-KRAB in a 24 well plate. Seventy-two hours or 6 days following transfection, cells were trypsinized and analyzed by flow cytometry using an LSR-II (BD Biosciences) and/or replated for the 6 day time point. mCherry bright cells were gated and EGFP levels were measured in this population.

Immunostaining

Cells were fixed in 4% paraformaldehyde, permeabilized with 0.5% NP-40 in phosphate buffered saline (PBS) for 10 min, washed with PBS for 5 min, blocked in 0.2% cold water fish gelatin and 0.5% bovine serum albumin (BSA) for 20 min, incubated with the primary antibody in blocking buffer at 4° overnight, washed three times and then incubated with Alexa647-conjugated secondary antibody at room temperature for 1 hr, washed again, and stained with DAPI. Primary and secondary antibodies used in this study were anti-TRF2 (E-20, sc-32106, Santa Cruz Biotechnology) and anti-53BP1 (Novex, NB100-304).

SUPPLEMENTAL INFORMATION

Supplemental Information includes Extended Experimental Procedures, six figures, and five movies and can be found with this article online at http://dx.doi.org/10.1016/j.cell.2013.12.001.

ACKNOWLEDGMENTS

The authors thank Cell Line Genetics for karyotype analysis. B.C., W.Z. and B.H. acknowledge support from the California Institute for Quantitative Biomedical Research (QB3) and the UCSF Program for Breakthroughs in Biomedical Research. L.S.Q. acknowledges support from the UCSF Center for Systems and Synthetic Biology, NIH Office of The Director (OD), and National Institute of Dental & Craniofacial Research (NIDCR). J.S. acknowledges support from a Boehringer Ingelheim Fonds Ph.D. fellowship. This work was in part supported by NIH P50 (grant GM081879, L.S.Q.), NIH Director's Early Independence Award (grant OD017887, L.S.Q.), NIH R01 (grant DA036858, L.S.Q. and J.S.W.), NIH P50 (grant GM102706, J.S.W), NIH U01 (grant CA168370, J.S.W), NIH R01 (grant CA096840, E.H.B. and B.A.C.), the Leukemia and Lymphoma Society (L.A.G.), the Helen Hay Whitney Foundation (G.W.L.), NIH Pathway to Independence Award (GM105913, G.W.L.), and the Howard Hughes Medical Institute (L.A.G., G.L., J.P. and J.S.W).

Received: October 30, 2013
Revised: November 25, 2013
Accepted: December 3, 2013
Published: December 19, 2013

REFERENCES

Augui, S., Nora, E.P., and Heard, E. (2011). Regulation of X-chromosome inactivation by the X-inactivation centre. Nat. Rev. Genet. *12*, 429–442.

Barrangou, R., Fremaux, C., Deveau, H., Richards, M., Boyaval, P., Moineau, S., Romero, D.A., and Horvath, P. (2007). CRISPR provides acquired resistance against viruses in prokaryotes. Science *315*, 1709–1712.

Cong, L., Ran, F.A., Cox, D., Lin, S., Barretto, R., Habib, N., Hsu, P.D., Wu, X., Jiang, W., Marraffini, L.A., and Zhang, F. (2013). Multiplex genome engineering using CRISPR/Cas systems. Science *339*, 819–823.

Cremer, T., and Cremer, M. (2010). Chromosome territories. Cold Spring Harb. Perspect. Biol. *2*, a003889.

d'Adda di Fagagna, F., Reaper, P.M., Clay-Farrace, L., Fiegler, H., Carr, P., Von Zglinicki, T., Saretzki, G., Carter, N.P., and Jackson, S.P. (2003). A DNA damage checkpoint response in telomere-initiated senescence. Nature *426*, 194–198.

Deltcheva, E., Chylinski, K., Sharma, C.M., Gonzales, K., Chao, Y., Pirzada, Z.A., Eckert, M.R., Vogel, J., and Charpentier, E. (2011). CRISPR RNA maturation by trans-encoded small RNA and host factor RNase III. Nature *471*, 602–607.

Dimitrova, N., Chen, Y.C., Spector, D.L., and de Lange, T. (2008). 53BP1 promotes non-homologous end joining of telomeres by increasing chromatin mobility. Nature *456*, 524–528.

Esvelt, K.M., Mali, P., Braff, J.L., Moosburner, M., Yaung, S.J., and Church, G.M. (2013). Orthogonal Cas9 proteins for RNA-guided gene regulation and editing. Nat. Methods *10*, 1116–1121.

Fraser, P., and Bickmore, W. (2007). Nuclear organization of the genome and the potential for gene regulation. Nature *447*, 413–417.

Gaj, T., Gersbach, C.A., and Barbas, C.F., 3rd. (2013). ZFN, TALEN, and CRISPR/Cas-based methods for genome engineering. Trends Biotechnol. *31*, 397–405.

Gendler, S.J., Lancaster, C.A., Taylor-Papadimitriou, J., Duhig, T., Peat, N., Burchell, J., Pemberton, L., Lalani, E.N., and Wilson, D. (1990). Molecular cloning and expression of human tumor-associated polymorphic epithelial mucin. J. Biol. Chem. *265*, 15286–15293.

Gerlich, D., Beaudouin, J., Kalbfuss, B., Daigle, N., Eils, R., and Ellenberg, J. (2003). Global chromosome positions are transmitted through mitosis in mammalian cells. Cell *112*, 751–764.

Gilbert, L.A., Larson, M.H., Morsut, L., Liu, Z., Brar, G.A., Torres, S.E., Stern-Ginossar, N., Brandman, O., Whitehead, E.H., Doudna, J.A., et al. (2013). CRISPR-mediated modular RNA-guided regulation of transcription in eukaryotes. Cell *154*, 442–451.

Grewal, S.I., and Jia, S. (2007). Heterochromatin revisited. Nat. Rev. Genet. *8*, 35–46.

Griffith, J.D., Comeau, L., Rosenfield, S., Stansel, R.M., Bianchi, A., Moss, H., and de Lange, T. (1999). Mammalian telomeres end in a large duplex loop. Cell *97*, 503–514.

Hellwig, D., Münch, S., Orthaus, S., Hoischen, C., Hemmerich, P., and Diekmann, S. (2008). Live-cell imaging reveals sustained centromere binding of CENP-T via CENP-A and CENP-B. J Biophotonics *1*, 245–254.

Heun, P., Laroche, T., Shimada, K., Furrer, P., and Gasser, S.M. (2001). Chromosome dynamics in the yeast interphase nucleus. Science *294*, 2181–2186.

Hollingsworth, M.A., and Swanson, B.J. (2004). Mucins in cancer: protection and control of the cell surface. Nat. Rev. Cancer *4*, 45–60.

Hsu, P.D., Scott, D.A., Weinstein, J.A., Ran, F.A., Konermann, S., Agarwala, V., Li, Y., Fine, E.J., Wu, X., Shalem, O., et al. (2013). DNA targeting specificity of RNA-guided Cas9 nucleases. Nat. Biotechnol. *31*, 827–832.

Hultdin, M., Grönlund, E., Norrback, K., Eriksson-Lindström, E., Just, T., and Roos, G. (1998). Telomere analysis by fluorescence in situ hybridization and flow cytometry. Nucleic Acids Res. *26*, 3651–3656.

Jinek, M., Chylinski, K., Fonfara, I., Hauer, M., Doudna, J.A., and Charpentier, E. (2012). A programmable dual-RNA-guided DNA endonuclease in adaptive bacterial immunity. Science *337*, 816–821.

Jinek, M., East, A., Cheng, A., Lin, S., Ma, E., and Doudna, J. (2013). RNA-programmed genome editing in human cells. Elife *2*, e00471.

Kim, S.H., Kaminker, P., and Campisi, J. (1999). TIN2, a new regulator of telomere length in human cells. Nat. Genet. *23*, 405–412.

Langer-Safer, P.R., Levine, M., and Ward, D.C. (1982). Immunological method for mapping genes on Drosophila polytene chromosomes. Proc. Natl. Acad. Sci. USA *79*, 4381–4385.

Larson, M.H., Gilbert, L.A., Wang, X., Lim, W.A., Weissman, J.S., and Qi, L.S. (2013). CRISPR interference (CRISPRi) for sequence-specific control of gene expression. Nat. Protoc. *8*, 2180–2196.

Levi, V., Ruan, Q., Plutz, M., Belmont, A.S., and Gratton, E. (2005). Chromatin dynamics in interphase cells revealed by tracking in a two-photon excitation microscope. Biophys. J. *89*, 4275–4285.

Lichter, P., Tang, C.J., Call, K., Hermanson, G., Evans, G.A., Housman, D., and Ward, D.C. (1990). High-resolution mapping of human chromosome 11 by in situ hybridization with cosmid clones. Science *247*, 64–69.

Mali, P., Yang, L., Esvelt, K.M., Aach, J., Guell, M., DiCarlo, J.E., Norville, J.E., and Church, G.M. (2013). RNA-guided human genome engineering via Cas9. Science *339*, 823–826.

Meyer, B.J. (2010). Targeting X chromosomes for repression. Curr. Opin. Genet. Dev. *20*, 179–189.

Misteli, T. (2007). Beyond the sequence: cellular organization of genome function. Cell *128*, 787–800.

Misteli, T. (2013). The cell biology of genomes: bringing the double helix to life. Cell *152*, 1209–1212.

Miyanari, Y., Ziegler-Birling, C., and Torres-Padilla, M.E. (2013). Live visualization of chromatin dynamics with fluorescent TALEs. Nat. Struct. Mol. Biol. *20*, 1321–1324.

Moyzis, R.K., Buckingham, J.M., Cram, L.S., Dani, M., Deaven, L.L., Jones, M.D., Meyne, J., Ratliff, R.L., and Wu, J.R. (1988). A highly conserved repetitive DNA sequence, (TTAGGG)n, present at the telomeres of human chromosomes. Proc. Natl. Acad. Sci. USA *85*, 6622–6626.

Nasmyth, K., and Haering, C.H. (2009). Cohesin: its roles and mechanisms. Annu. Rev. Genet. *43*, 525–558.

Nielsen, S., Yuzenkova, Y., and Zenkin, N. (2013). Mechanism of eukaryotic RNA polymerase III transcription termination. Science *340*, 1577–1580.

Nollet, S., Moniaux, N., Maury, J., Petitprez, D., Degand, P., Laine, A., Porchet, N., and Aubert, J.P. (1998). Human mucin gene MUC4: organization of its 5′-region and polymorphism of its central tandem repeat array. Biochem. J. *332*, 739–748.

Onn, I., Heidinger-Pauli, J.M., Guacci, V., Unal, E., and Koshland, D.E. (2008). Sister chromatid cohesion: a simple concept with a complex reality. Annu. Rev. Cell Dev. Biol. *24*, 105–129.

Qi, L.S., Larson, M.H., Gilbert, L.A., Doudna, J.A., Weissman, J.S., Arkin, A.P., and Lim, W.A. (2013). Repurposing CRISPR as an RNA-guided platform for sequence-specific control of gene expression. Cell *152*, 1173–1183.

Robinett, C.C., Straight, A., Li, G., Willhelm, C., Sudlow, G., Murray, A., and Belmont, A.S. (1996). In vivo localization of DNA sequences and visualization of large-scale chromatin organization using lac operator/repressor recognition. J. Cell Biol. *135*, 1685–1700.

Roukos, V., Voss, T.C., Schmidt, C.K., Lee, S., Wangsa, D., and Misteli, T. (2013). Spatial dynamics of chromosome translocations in living cells. Science *341*, 660–664.

Sinclair, P., Bian, Q., Plutz, M., Heard, E., and Belmont, A.S. (2010). Dynamic plasticity of large-scale chromatin structure revealed by self-assembly of engineered chromosome regions. J. Cell Biol. *190*, 761–776.

van Steensel, B., and Dekker, J. (2010). Genomics tools for unraveling chromosome architecture. Nat. Biotechnol. *28*, 1089–1095.

Wang, X., Kam, Z., Carlton, P.M., Xu, L., Sedat, J.W., and Blackburn, E.H. (2008). Rapid telomere motions in live human cells analyzed by highly time-resolved microscopy. Epigenetics Chromatin *1*, 4.

Wang, W., Li, G.W., Chen, C., Xie, X.S., and Zhuang, X. (2011). Chromosome organization by a nucleoid-associated protein in live bacteria. Science *333*, 1445–1449.

Wang, H., Yang, H., Shivalila, C.S., Dawlaty, M.M., Cheng, A.W., Zhang, F., and Jaenisch, R. (2013). One-step generation of mice carrying mutations in multiple genes by CRISPR/Cas-mediated genome engineering. Cell *153*, 910–918.

Wiedenheft, B., Sternberg, S.H., and Doudna, J.A. (2012). RNA-guided genetic silencing systems in bacteria and archaea. Nature *482*, 331–338.

Xu, L., and Blackburn, E.H. (2007). Human cancer cells harbor T-stumps, a distinct class of extremely short telomeres. Mol. Cell *28*, 315–327.